Numerical Simulation and Analysis of Crosswind Inlet Flows at Low Mach numbers

Yann Colin, Betrand Aupoix, Jean-François Boussuge, Philippe Chanez

Proceedings of the 8th International Symposium
on Experimental and Computational
Aerothermodynamics of Internal Flows
Lyon, July 2007
Paper reference: ISAIF8-0058

Numerical Simulation and Analysis of Crosswind Inlet Flows at Low Mach numbers

Y. Colin[a,*], B. Aupoix[b], J.F. Boussuge[a] and P. Chanez[c]

[a]CERFACS, CFD Team, 42 Av. G. Coriolis, 31057 Toulouse Cedex, France
[b]ONERA DMAE, 2 Av. Edouard Belin, 31055 Toulouse, France
[c]SNECMA, Villaroche, 77550 Moissy-Cramayel, France

The study is motivated by the need of engine designers to have a robust, accurate and efficient tool able of simulating complex flows around and inside an isolated, or close to the ground, nacelle in a crosswind. The code has to compute both incompressible and transonic zones and consequently a low-speed preconditioning method is required. Such separated flows exhibit considerable hysteresis in the separation and reattachment processes into the intake. This phenomenon was successfully solved by using dual time stepping integration. Lastly, six eddy-viscosity turbulence models frequently employed for aeronautical flows have been compared to assess their predictive accuracy in computing complex three-dimensional separated flows. It is found that the one-equation model of Spalart-Allmaras and the k-ω SST model of Menter are the only models able to predict separated flows at high subsonic engine mass flowrate.

Keywords: Low-speed preconditioning, crosswind inlet flows, separation hysteresis, turbulence modeling.

Introduction

Nacelles design must fulfill geometrical constraints and engine requirements. One of the engine requirements is focused notably on the homogeneity of the flow in front of the fan which is quantified by the distortion levels of the total pressure in this plane. Airplane on the ground with crosswind is a critical case for the nacelle. Subsonic or supersonic separations occur in the inlet, according to the engine mass flowrate. The resulting heterogeneity of the flow may account for the outbreak of aerodynamic instabilities of the fan blades and, if the distortion is large enough, the fan might stall. CERFACS, in collaboration with Snecma and ONERA, is working on the numerical simulation of such crosswind inlet flows in order to predict these distortion levels. Such crosswind flows exhibit three distinctive features challenging from a numerical and a modeling point of view.

Firstly, this application is featured by the cohabitation of incompressible and transonic areas around the inlet lip. Indeed the infinite crosswind velocity varies between 20 and 35 kt which yield Mach numbers of the order of 10^{-2} whereas the Mach number may be superior to unity at the inlet lip. It turns out that the convergence of the pseudo-unsteady methods applied to the system of the Euler or Navier-Stokes equations in compressible flow is

*corresponding author
E. Mail Yann.Colin@cerfacs.fr

Nomenclature

nradius	Number of crowns	*VNN*	von Neumann number
S_i	i-th crown section	*M*	Mach number
R_i	i-th crown radius	M_{lim}	Limit Mach number
P	Fan plane average pressure (Pa)	M_r	Reference Mach number
P_i	Average pressure on i-th crown (Pa)	M_{is}	Isentropic Mach number
IDC	Circumferential distortion index	c	Speed of sound
MFR	Mass flowrate (kg/s)	**Greek letters**	
W	State vector in conservative variables	θ	Fan plane circumferential angle
U	Euler symmetrizing variables vector	ε	Preconditioning parameter
F	Flux tensor	δ	Weiss-Smith parameter
f,g,h	Convective fluxes	σ_{pgr}	Pressure-gradient free parameter
f_v,g_v,h_v	Viscous fluxes	β	M_r scaling factor
Γ_W	Generic preconditioner in conservative form	ρ	Density
Γ	Generic preconditioner in Euler symmetrizing form	ν	Kinematic viscosity
D	Jameson artificial dissipation flux	γ	Specific-heat ratio
A	Jacobian matrix of the convective flux	**Subscripts**	
CFL	Courant-Friedrichs and Lewy number	*min*	Minimum value

degraded at low velocities. This performance loss is due to the large disparity between the fast acoustic modes and the slow convective modes. Local preconditioning procedures [1-5] in which the time derivatives of the compressible equations are altered to control the eigenvalues and to accelerate convergence have been used.

The second flow feature of this application is the considerable hysteresis phenomenon occurring in the separation and reattachment processes as the engine mass flowrate evolves. This behavior has been experimentally highlighted by Raynal [6] or Quemard et al. [7]. They indicate that large hysteresis can be observed when testing model intakes by varying angles of attack. Recently, Hall and Hynes [8] carefully measured the hysteresis associated with separation and reattachment and showed that it is particularly sensitive to fan operating point and the location of the ground plane. At present there are few theoretical bases for analyzing aerodynamic hysteresis and it remains a difficult phenomenon to examine numerically. This phenomenon has been successfully reproduced in this study by using dual time stepping integration.

Lastly, crosswind intake flows feature complex three-dimensional separations starting from the leading edge of the nacelle down to the fan. Fast and accurate computations are required by engineers in nacelles design context. Therefore computational predictions for such flows are obtained by solving the Reynolds-averaged Navier-Stokes equations in combination with eddy-viscosity turbulence models. Six eddy-viscosity turbulence models are considered to assess their efficiency in computing separated intake flows for different engine mass flowrates.

The present work thus aims to assess some numerical tools to compute crosswind inlet flows at low-Mach numbers along with separation hysteresis phenomena.

Problem description and experimental setup

Experimental apparatus

In order to characterize the intake separation area and to quantify the heterogeneity of the flow in front of the fan plane, Snecma intensively uses experimental tests. The experimental setup tested at the F1 ONERA Fauga wind tunnel is illustrated in Fig. 1. The nacelle is set vertically and different crosswind velocities (from 20 to 35 kt) are considered for the entire engine flowrate range (Mass flowrates varying from 0 to 1300 kg/s).

Steady total pressure probes are allocated in the fan plane on eight arms at five different radii illustrated in Fig. 2. The probe locations are summarized in Tab. 1 and give some information about the spatial evolution of pressure distribution.

Distortion levels definition

The influence of the total pressure distortion is generally studied with the introduction of the circumferential distortion index (IDC) to characterize the heterogeneity of the flow. This coefficient is defined as

$$IDC = \underset{i=1}{\overset{nradius-1}{MAX}} \left(0.5 \left[\frac{(\overline{P_i} - Pmin_i)}{\overline{P}} + \frac{(\overline{P_{i+1}} - Pmin_{i+1})}{\overline{P}} \right] \right) \quad (1)$$

where P is the average pressure and Pmin the minimal pressure of the i-th crown. This index is devoted to assess the effect of the intake flow on the stability of the fan and enables to define surge margin.

The experiment conducted by ONERA consists of measuring the distortion in the fan plane as the mass flowrate (MFR) increases. Then the evolution of the distortion in terms of the flowrate may be represented, as

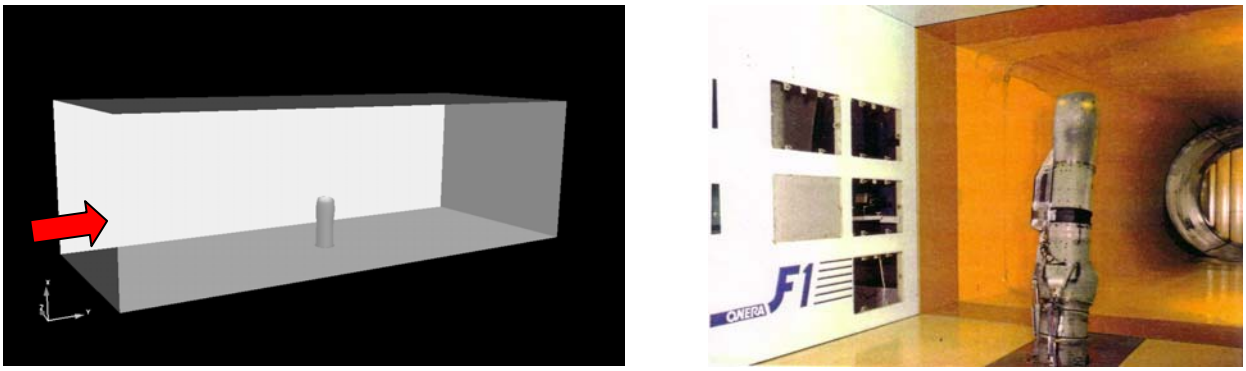

Fig. 1: Crosswind tests at the F1 ONERA Fauga wind tunnel.

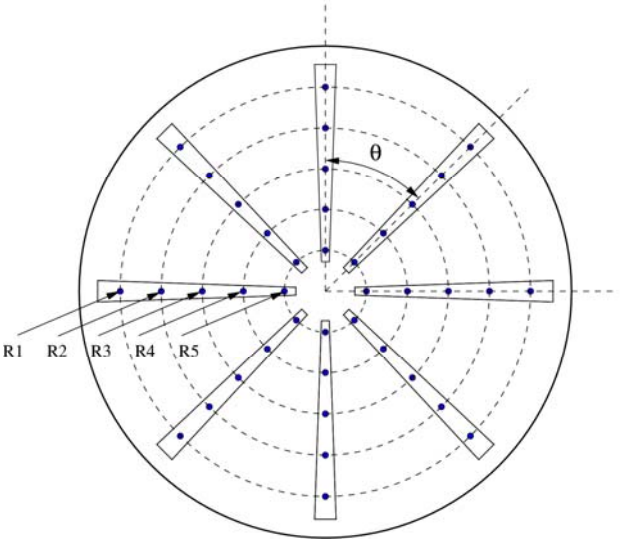

Fig. 2 Distortion measuring system.

Crown i	Si/S_{tot}	Ri/R_{ext}
1	0.1	0.3162
2	0.3	0.5477
3	0.5	0.7071
4	0.7	0.8367
5	0.9	0.9487

Tab. 1 Location of the crowns.

depicted in Fig. 3. At low MFR, subsonic separation takes place in the intake. As MFR increases, the separation extent tends to reduce but total pressure losses become higher, resulting in IDC increase. At intermediate MFR (between 850 and 1000 kg/s for Lara nacelle), the boundary layer reattaches in the diffuser which leads to the IDC drop. The flow is homogeneous in front of the fan plane and this flowrate range defines the working range. Then, at high MFR, the flow becomes supersonic on the lip and brings about a shock wave associated with strong total pressure losses, which explains the sudden increase of the IDC coefficient. This shock wave may induce a separation of the boundary layer: the resulting high heterogeneity of the flow causes aerodynamic

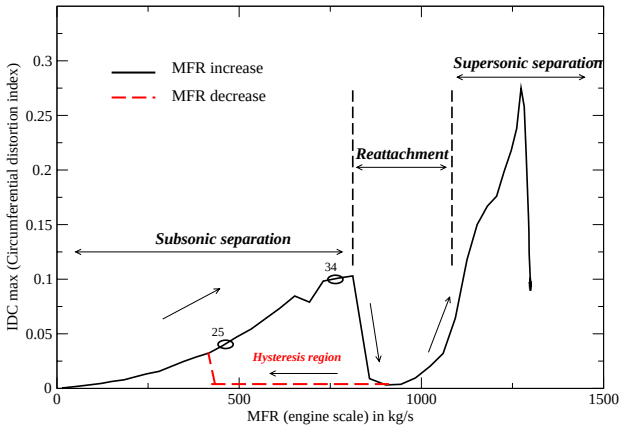

Fig. 3 Evolution of IDC versus mass flowrate.

instabilities responsible for strong vibrations which can damage the fan blades or lead to surge.

Governing equations and flow solver

Navier-Stokes equations

The governing equations are the unsteady compressible Navier-Stokes equations which describe the conservation of mass, momentum and energy of the flow field. In conservative form, they can be expressed in three-dimensional Cartesian coordinates (x,y,z) as:

$$\frac{\partial W}{\partial t} + div\mathcal{F} = 0 \qquad (2)$$

where $\mathcal{F} = (f - f_v, g - g_v, h - h_v)$ is the flux tensor. f, g, h are the inviscid fluxes and f_v, g_v, h_v are the viscous fluxes. For Reynolds-Averaged Navier-Stokes equations (RANS) the viscous fluxes involve turbulent fluxes which are modeled with classical eddy viscosity assumptions.

Flow solver

For this study, the elsA code [9] is used. This code is

jointly developed by ONERA in Chatillon and CERFACS in Toulouse and supported by Airbus and Snecma. The elsA code solves the compressible Navier-Stokes equations using a finite volume method with various spatial discretization schemes like Jameson's central difference scheme [10], Roe's scheme [11] or HLLC scheme [12].

Low-speed preconditioning techniques

Convergence enhancement

Preconditioning techniques involve the alteration of the time-derivatives used in time-marching CFD methods with the primary objective of enhancing their convergence. The original motivation for the development of these techniques arose from the need to compute low speed compressible flows efficiently. At low Mach numbers, the performances of traditional time-marching algorithms suffer because of the wide disparity that exists between the particle and acoustic wave speeds. Preconditioning methods introduce artificial time-derivatives which alter the acoustic waves so that they travel at speeds that are comparable in magnitude to the particle waves. Thereby good convergence characteristics may be obtained at all speeds. The alteration of the propagation velocities is done by multiplying the time-derivative of Eq.(2) by a preconditioning matrix Γ_W as follows:

$$\Gamma_W \frac{\partial W}{\partial t} + div\mathcal{F} = 0 \tag{3}$$

A generic Weiss-Smith/Choi-Merkle preconditioner based on Merkle/Weiss workgroups [1,4,5] was implemented and validated in elsA. Using the Euler symmetrizing variables dU=[dp/ρc, du, dv, dw, dS], the preconditioner can be written as follows:

$$\Gamma = \begin{pmatrix} \frac{1}{\varepsilon} & 0 & 0 & 0 & \frac{\delta}{\rho c} \\ 0 & 1 & 0 & 0 & 0 \\ 0 & 0 & 1 & 0 & 0 \\ 0 & 0 & 0 & 1 & 0 \\ 0 & 0 & 0 & 0 & 1 \end{pmatrix} \tag{4}$$

where ε is the preconditioning parameter and δ is a free parameter varying from 0 to 1. For δ=0, the preconditioner is the Weiss-Smith preconditioner, which is a member of Turkel's family. The preconditioning parameter is initially defined as:

$$\varepsilon = \mathrm{Min}(1, \mathrm{Max}(M_{lim}^2, M^2)) \tag{5}$$

Where M_{lim} is set to 10^{-5} to prevent singularities at solid walls and the above formulation yields ε=1 for Mach numbers greater than one.

Robustness Aspects

It turns out that the use of preconditioning techniques greatly reduces the robustness of the flow solver. Numerical test cases show that the preconditioning parameter ε is the critical factor influencing robustness issues. Two cases may be distinguished, requiring special treatment.

Firstly, for Euler computations, the lack of robustness arises when the Mach number locally approaches zero near a stagnation point. Darmofal and Siu [13] suggest reducing locally ε in such regions as follows:

$$\varepsilon = \mathrm{Min}(1, \mathrm{Max}(M_{lim}^2, M^2, \sigma_{pgr}\frac{|\Delta p|}{\rho c^2})) \tag{6}$$

where σ_{pgr} is a free case-dependent parameter.

Then, for turbulent computations, the lack of robustness is due to low Reynolds number regions. Preconditioning techniques are devoted to eliminate analytic stiffness, arising from propagative disparities in the limit of vanishing Mach number, inherent to the hyperbolic system of Euler equations. However, for viscous-dominated flows, where the system becomes parabolic, the region in boundary layers is dominated by diffusion processes. Thus the formulation (5) for ε may lead to too large time steps in these regions. Venkateswaran and Merkle [5] suggest introducing the local diffusion velocity ν/Δh and to reduce ε in the following way:

$$\varepsilon = \mathrm{Min}(1, \mathrm{Max}(M_{lim}^2, M^2, \left(\frac{\nu}{c\Delta h}\right)^2)) \tag{7}$$

where Δh is a proper diffusion length scale based on the mesh distribution. The advantage of this formulation is that it equalizes the acoustic CFL number with the VNN number. Unfortunately, this restriction turns to be inefficient for conducting intake separation computations. A much more robust formulation suggested by Turkel [14] was implemented:

$$\varepsilon = \mathrm{Min}(1, \mathrm{Max}(M_{lim}^2, M^2, \beta M_r^2)) \tag{8}$$

M_r is usually taken as the inflow Mach number so that ε becomes constant in the boundary layer region. β ≈ 3-5 depending up on mass flowrates. The problematic of this restriction is the prescription of the reference Mach number. For crosswind inlet flows, the boundary layer expands at very low Mach numbers whereas it develops at much higher Mach numbers in the intake. This is why a restriction based on isentropic Mach number has been introduced as follows:

$$\varepsilon = \mathrm{Min}(1, \mathrm{Max}(M_{lim}^2, M^2, M_{is}^2)) \tag{9}$$

with

$$M_{is}^2 = \frac{2}{\gamma - 1}\left[\left(\frac{pt_\infty}{p}\right)^{\frac{\gamma}{\gamma-1}} - 1\right] \qquad (10)$$

Given the fact that the normal pressure gradient is zero in the boundary layer, M_{is} is pretty constant in this region and is equal to the Mach number at the boundary layer interface.

Lastly, when all these restrictions are combined, the determination of ε is implemented as follows:

$$\varepsilon = \mathrm{Min}(1, \mathrm{Max}(M_{lim}^2, M^2, \sigma_{pgr}\frac{|\Delta p|}{\rho c^2}, \beta M_r^2, M_{is}^2)) \qquad (14)$$

Artificial dissipation models

The use of preconditioning does not only reduce the stiffness of the system of equations, it also improves accuracy at low speeds. Turkel et al. [15] showed that the loss of accuracy of the original convective schemes is due to an ill-conditioning of artificial dissipation fluxes which become extremely large for very low velocities. The modification of the fluxes required to take into account the new characteristics of the preconditioned system results in a well conditioned dissipation formulation and ensures reliable accuracy. In the present work, the scalar artificial dissipation of Jameson et al. [10], Roe and HLLC schemes have been modified.

The artificial dissipation flux D of Jameson et al. consists of a blend of second- and fourth- order differences. Within the finite volume method D is defined at the interface i+1/2 as:

$$\begin{aligned} D_{i+1/2} &= \epsilon^{(2)}_{i+1/2}(W_{i+1} - W_i) \\ &\quad -\epsilon^{(4)}_{i+1/2}(W_{i+2} - 3W_{i+1} + 3W_i - W_{i-1}) \end{aligned} \qquad (11)$$

The coefficients $\varepsilon^{(2)}$ and $\varepsilon^{(4)}$ are used to locally adapt the dissipative flux and are directionally scaled by the scaling factor $r_{i+1/2}$:

$$\begin{aligned} \varepsilon^{(2)}_{i+1/2} &= k^{(2)}\, r_{i+1/2}\, \nu_{i+1/2} \\ \varepsilon^{(4)}_{i+1/2} &= \max(0\,,\, k^{(4)}\, r_{i+1/2} - \varepsilon^{(2)}_{i+1/2}) \end{aligned} \qquad (12)$$

The scaling factor $r_{i+1/2}$ is calculated as the average of the spectral radii at the cell face

$$r_{i+1/2} = \frac{1}{2}(\lambda(\Gamma_W^{-1}A)_i^I + \lambda(\Gamma_W^{-1}A)_{i+1}^I) \qquad (13)$$

where $\lambda(\Gamma_W^{-1}A)$ is the spectral radius of the preconditioned Jacobian matrix. The order of magnitude of the factor $r_{i+1/2}$ is now the flow velocity and not the speed of sound as in the original model. However, as explained above, the preconditioning parameter ε has been reduced in the boundary layer for stiffness issues, which may account for high values of artificial dissipation close to the wall. Thus the strategy consists of damping the artificial dissipation D near the wall by multiplying this flux by $(M/M_{is})^2$.

The modification of Roe and HLLC scheme follows the procedure described in [16] and [17] respectively. Numerical studies showed that the use of such upwind schemes led to too much dissipative solutions, notably predicting reattachment mass flowrates which are much lower than the one inferred from experimental data. Numerical computations presented next use preconditioned centered Jameson scheme along with artificial dissipation damping.

Hysteresis simulation: Unsteady time integration

As pointed out above, crosswind inlet flows exhibit considerable hysteresis in the separation and reattachment processes as the engine mass flowrate evolves. As illustrated in Fig. 3, when the flow is separated, increasing the mass flowrate tends to reduce the separated area, bringing the flowfield closer to reattachment. Once the flow is reattached, if the mass flowrate is reduced, separation occurs at a much lower flowrate than that required for reattachment. At present, theoretical bases for analyzing aerodynamic hysteresis are not well developed and it remains a difficult phenomenon to investigate numerically.

In our study, it turns out that steady computations failed to yield steady distortion in fan plane. Indeed these methods, involving local time stepping or preconditioning procedures alter time derivatives of the original equations. The loss of time consistency in the hysteresis region may account for the inefficiency of these methods.

On the contrary, unsteady time integration techniques such as Gear or Dual Time Stepping (DTS) methods were successful in converging to a steady separated solution. Fig. 4 shows the hysteresis phenomenon simulation realized with DTS time integration and the k-ω BSL model of Menter. The simulation is done by running a series of increasing MFR until reattachment of the flow.

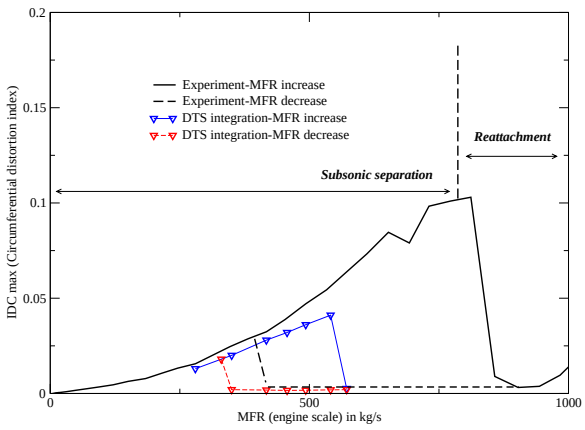

Fig. 4 Hysteresis simulation with DTS integration technique.

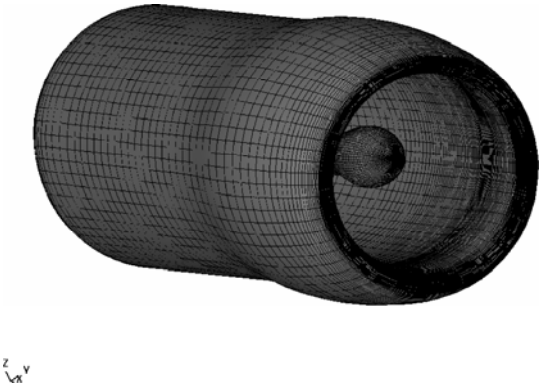

Fig. 5 Partial view of the 3D Lara nacelle mesh.

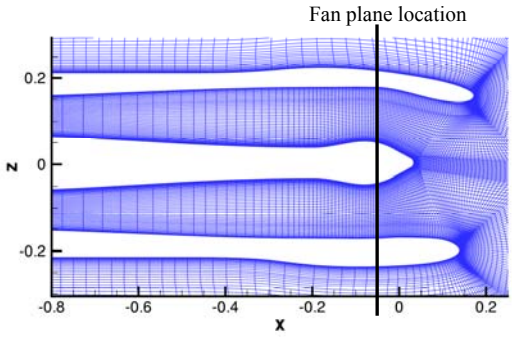

Fig. 6 2D cut in xOz plane.

Then a series of decreasing MFR simulations is done until separation of the flow. This technique enables to capture the two possible states of the flow field for a given flowrate.

Simulation of subsonic separation and reattachment

The configuration provided by Snecma consists of the Lara nacelle which has been tested at the F1 ONERA wind tunnel. The computational domain, illustrated in Fig. 1, is designed to match the wind tunnel facilities. A crosswind velocity of 30 kt (corresponding to a Mach number of 0.04) and a Reynolds number of 4.5 10^6 are considered while an outflow condition is imposed downstream of the fan plane using a constant static pressure lower than the freestream one. The simulation is conducted by running a series of increasing MFR until reattachment of the flow may be observed.

Meshing strategy

The mesh is generated using ICEM-CFD software and a global view of the nacelle is represented in Fig. 5. Fig. 6 shows parts of the C-mesh around the nacelle, which is suitable to treat boundary layer separation. In order to avoid interaction of the separation in the intake with the boundary condition, the outlet condition is imposed far more inside the inlet than in the wind tunnel test.

The fine Euler mesh is a structured multi-block mesh with 32 blocks and contains about 3.5 million grid points. The viscous grid is generated by remeshing the Euler grid close to the walls such that the first cell height in wall unit, based upon the internal Reynolds number, is lower than unity. The simulation of a large range of flowrates leads to generate a specific viscous mesh for each MFR. Sensitivity study showed that 40 points are required in the wall normal direction resulting in a final viscous mesh with 5.2 million grid points.

Comparison of eddy-viscosity turbulence models

In the present study, we mainly focus on transport-equation models. These models are presently very popular in computational fluid-dynamics applications and constitute the aircraft industry's "work horses". A total of six different models is considered. They range from the algebraic Baldwin-Lomax model [16] over the Spalart-Allmaras (SA) one-equation model [17] to three different two-equation k-ω models (k-ω 1988 by Wilcox [18], k-ω BSL and SST by Menter [19]). In addition, the k-l model of Smith [20] is also investigated. We have not included a classical k-ε model in our study because its deficiencies for predicting aerodynamic flows with adverse pressure gradients are well known [21-22].

All these models have been tested on the Lara nacelle to assess their ability to predict accurate solution as the flow separates. The results are presented for two engine mass flowrates of 450 and 800 kg/s corresponding respectively to points 25 and 34 of the experiment as illustrated in Fig. 3. Firstly, wall isentropic Mach repartitions are computed at four angular positions 0°, 45°, 90° and 135° as illustrated in Fig. 8 (a) for both external and in-

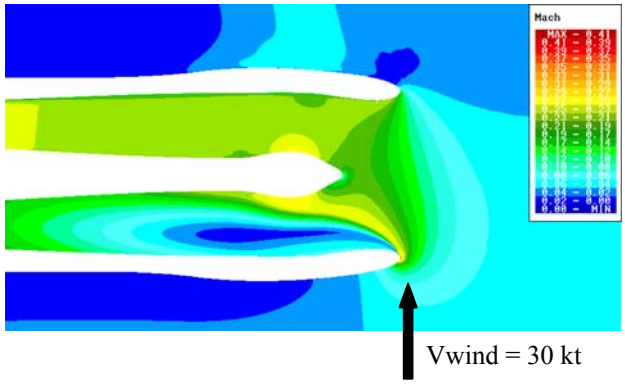

Fig. 7 Mach isocontours at PT25 with SA model

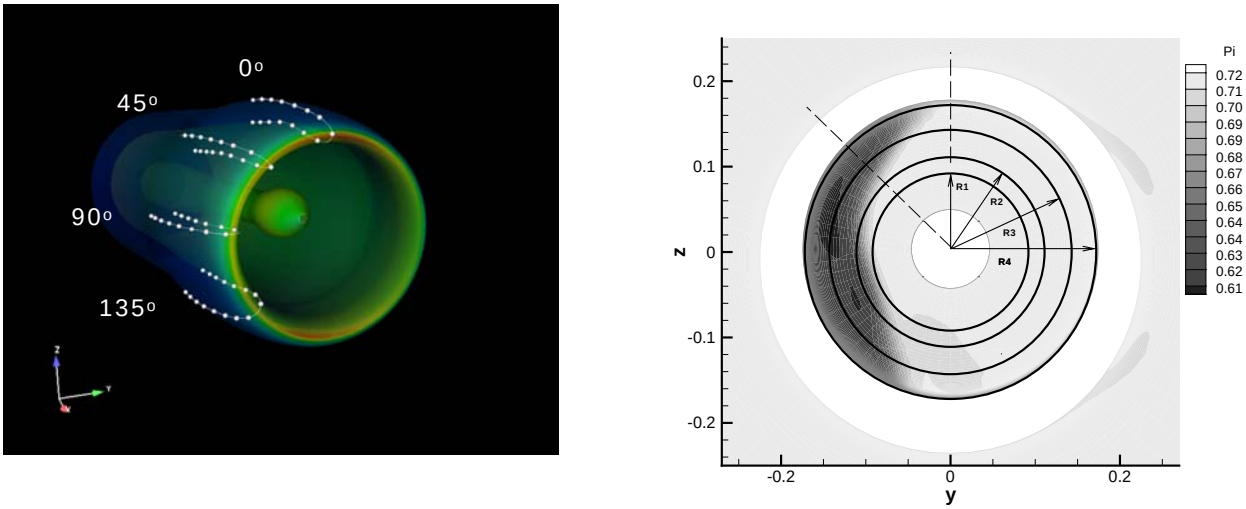

(a) (b)

Fig. 8 Repartition of the probes to extract (a) wall isentropic Mach and (b) fan plane total pressure distributions.

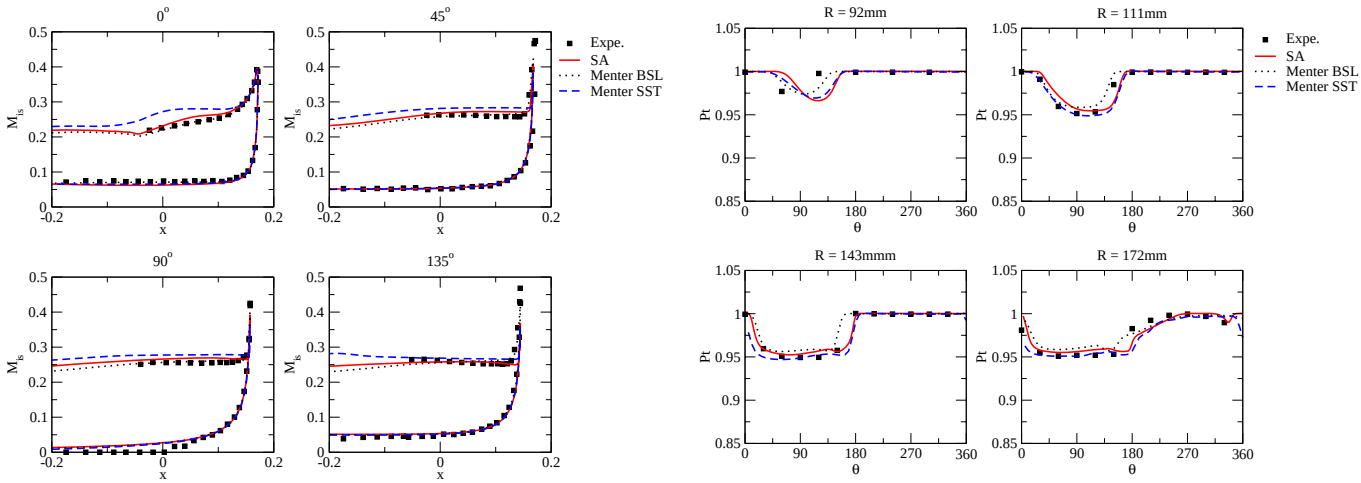

(a) (b)

Fig. 9 Wall isentropic Mach (a) and fan plane total pressure (b) distributions at PT25.

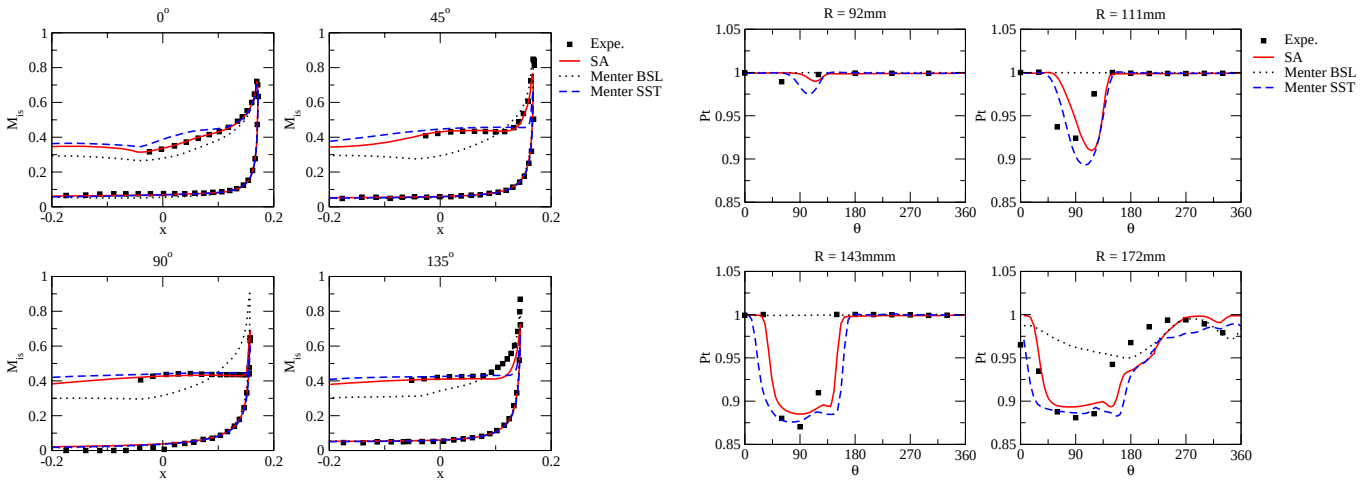

(a) (b)

Fig. 10 Wall isentropic Mach (a) and fan plane total pressure (b) distributions at PT34.

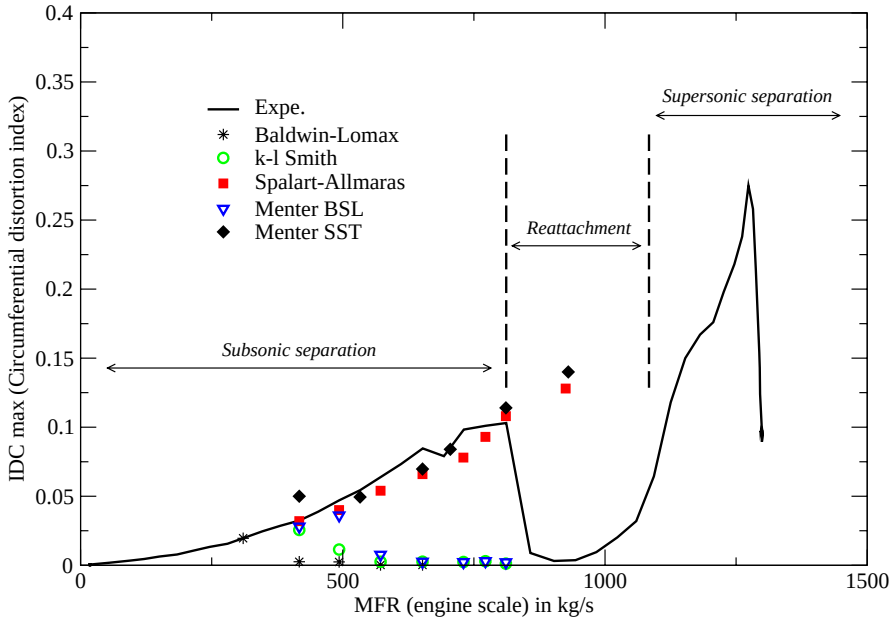

Fig. 11 Estimation of IDC with increasing MFR for a 30kt crosswind speed.

ternal flows. The crosswind direction is following the y-axis direction. Besides, total pressure drops are plotted in terms of the circumferential angle θ as described in Fig. 8(b) and yield details on the three-dimensional separation extent. Results for SA, BSL and SST models are presented only, but an overall comparison will be made with Fig. 11.

Figure 9 compares these three models at PT25, corresponding to a MFR of 450kg/s, where a massive separation takes place as illustrated in Fig. 7. Fig. 9(b) shows that the separation extends from $\theta=0^o$ to 180^o, with quite weak pressure drops of about 5% which result in a small value of IDC. SA and SST models tend to slightly overestimate the separation extent and the pressure drop. A consequence is the underestimation of the Mach peak values on the lips at 45^o and 135^o for these two models. BSL model predicts the lowest isentropic Mach plateau at 45^o, 90^o and 135^o and is therefore in closest agreement with the experiment.

Figure 10 compares the same models at PT34, corresponding to a MFR of 800 kg/s. Increasing the engine flowrate leads to a reduction of the separation area in the intake but also to a growth of total pressure losses (Fig. 10(b)) of about 10%. The flowrate corresponding to PT34 is slightly inferior to the expected reattachment flowrate. Therefore, it is a challenging test case for the assessment of turbulence model behavior in separated flow. Indeed BSL model predicts a reattachment of the boundary layer for much lower flowrates. The isentropic Mach distribution is linearly decreasing which is a feature for reattached boundary layer. Moreover, no total pressure drop may be seen in Fig. 10(b). On the contrary, SST correction overestimates the separated area extent, especially at the angular positions $\theta= 45^o$ and 135^o in Fig. 10(a) or in the fan plane at the radii R=143 and 172 mm in Fig. 10(b). SA model is finally a "good" compromise between the last two ones.

Fan plane distortion

To summarize the efficiency of the different turbulence models presented above, the IDC coefficient is plotted in Fig. 11 in the subsonic range for an increasing MFR. The Baldwin-Lomax, k-l and k-ω BSL models predict reattachment mass flowrates which are much lower than the one inferred from experimental data. The k-ω 1988 model of Wilcox is not represented in Fig. 11 but yields results very similar to the k-ω BSL model of Menter. The Spalart-Allmaras and k-ω SST models on the contrary predict a separation zone that extends further than in the experiment, which may account for the failure of reattached flow prediction.

Summary and conclusions

A method to compute crosswind inlet flows at low Mach numbers has been presented. The stress is put on three distinctive flow features. Firstly the cohabitation of incompressible zones outside the nacelle along with

compressible ones in the intake has been computed using a generic Weiss-Smith/Choi-Merkle preconditioner. The computation of the preconditioning parameter turned out to be essential for ensuring a robust tool capable of simulating such flows. Then, the hysteresis phenomenon occurring in the separation and reattachment process was successfully solved by using Dual Time Stepping integration techniques. Last, assessment of turbulence-model performance was pursued for the prediction of intake separation. For this purpose, a comparative study of six eddy-viscosity turbulence models was performed.

It was found that none of these models was fully satisfactory. Baldwin-Lomax, k-l, k-ω and BSL models predict flow reattachment at much lower MFR than inferred from experimental data. Spalart-Allmaras and SST models are more accurate in separated flow regions but they fail to predict boundary-layer reattachment.

Acknowledgement

This investigation was supported by Snecma on behalf of Safran group.

References

[1] Choi,Y.H. and Merkle C.L.: The Application of Preconditioning in Viscous Flows, Journal of Computational Physics, vol.105, pp.207－223, (1993).

[2] Van Leer, B., Lee, W.T. and Roe, P.: Characteristic Time-Stepping or Local Preconditioning of the Euler Equations, AIAA paper 91-1552, (1991).

[3] Turkel, E., Radespiel, R. and Kroll, N.: Assessment of Preconditioning Methods for Multidimensional Aerodynamics, Computers & Fluids, vol.26, pp.613 － 634, (1997).

[4] Weiss, J.M. and Smith, W.A.: Preconditioning Applied to Variable and Constant Density Flows, AIAA Journal, vol.33, no.11, pp.2050－2057, (1995).

[5] Venkateswaran, S. and Merkle, L.: Analysis of Preconditioning Methods for the Euler and Navier-Stokes Equations, von Karman Institute for Fluid Dynamics, Lecture Series 1999-03, (1999).

[6] Raynal, J.C.: Lara Laminar Flow Nacelle Off-Design Performance Tests in the ONERA F1 Wind Tunnel, Test Report 4365AY178G, ONERA, Toulouse, France, (1994).

[7] Quemard, C., Garcon, F. and Raynal, J.C.: High Reynolds Number Air Intake Tests in the ONERA F1 Wind Tunnel, TP 1996-213, ONERA, Toulouse, France, (1996).

[8] Hall, C.A. and Hynes, T. P.: Measurements of Intake Separation Hysteresis in a Model Fan and Nacelle Rig, Journal of Propulsion and Power, vol.22, no.4, pp.872-879, (2006).

[9] L. Cambier and M. Gazaix: An Efficient Object-Oriented Solution to CFD Complexity, AIAA paper 2002-0108, (2002).

[10] Jameson, A., Schmidt, R. F. and Turkel, E.: Numerical Solutions of the Euler Equations by Finite Volume Methods Using Runge-Kutta Time Stepping, AIAA paper 81-1259, (1981).

[11] Roe, P.L.: Approximate Riemann Solvers, Parameter Vectors and Difference Schemes, Journal of Computational Physics, vol.43, pp.357－372, (1981).

[12] Toro, E.F., Spruce, M. and Speares, W.: Restoration of the Contact Surface in the HLL-Riemann Solver, Shock Waves, vol.4, pp.25－34, (1994).

[13] Darmofal, D.L. and Siu, K.: A Robust Multigrid Algorithm for the Euler Equations with Local Preconditioning and Semi-Coarsening, Journal of Computational Physics, vol.151, pp.728－756, (1999).

[14] Turkel, E.: Preconditioning Techniques in Computational Fluid Dynamics, Annual Review of Fluid Mechanics, vol.31, pp.385－416. (1999).

[15] Turkel, E., Fiterman, A. and van Leer, B.: Preconditioning and the Limit to the Incompressible Flow Equations, ICASE Report 93-42, (1993).

[16] Baldwin, B.S. and Lomax, H.: Thin Layer Approximation and Algebraic Model for Separated Turbulent Flows, AIAA paper 78-257, (1978).

[17] Spalart, P.R. and Allmaras, S.R.: A One-Equation Turbulence Transport Model for aerodynamic flows, AIAA Paper 92-0439, (1992).

[18] Wilcox, D.C.: Reassessment of the Scale-Determining Equation for Advanced Turbulence Models, AIAA Journal, vol.26, no.11, pp.1299－1310, (1988).

[19] Menter, F.R.: Two-Equation Eddy-Viscosity Turbulence Models for Engineering Applications, AIAA Journal, vol.32, no.8, pp.1598－1605, (1994).

[20] Smith, B.R.: A Near Wall Model for the k-l Two Equation Turbulence Model, AIAA Paper 94-2386, (1994).

[21] Rodi, W. and Sheuerer G.: Scrutinizing the k-ε Turbulence Model under Adverse Pressure Gradient Conditions, Journal of Fluids Engineering, vol.108, pp.174－179, (1986).

[22] Huang, P.G. and Bradshaw, P.: The Law of the Wall for Turbulent Flows in Pressure Gradients, AIAA Journal, vol.33, pp.624－632,(1995).